ASCE

Crack-Parallel Stress Effect on Fracture of Fiber-Reinforced Concrete Revealed by Gap Tests

Linfei Li[1]; Boning Wang[2]; Houlin Xu[3]; Hoang T. Nguyen[4]; Zdeněk P. Bažant, Dist.M.ASCE[5]; and Mija H. Hubler, A.M.ASCE[6]

Abstract: This paper presents an experimental study on how the crack-parallel stress affects the fracture properties of fiber-reinforced concrete (FRC) using the gap test—a new simple fracture test invented and used for concrete at Northwestern University in 2020. First, it was conducted for plain concrete and was successfully applied to cross-ply carbon-fiber composite and to aluminum. An advantage of this test is that it is unambiguous because the test setup changes from one statically determinate configuration to another. The gap test, combined with the standard notched three-point-bend test, is now applied to geometrically scaled FRC specimens to determine how the fracture energy, G_f, and the effective size, c_f, of the fracture process zone (FPZ), are changed by the crack-parallel stress, σ_{xx}. For σ_{xx} equal to about 2/3 of the standard uniaxial compression strength, the increase in G_f is 64% and 78% for the two FRCs, respectively, which is large but not as large as the 126% increase observed in tests of plain concrete. This indicates that the fiber reinforcement mitigates the effect of σ_{xx}, while introducing some degree of ductility into the fracture process. The compressive σ_{xx} also increases the effective size of the FPZ by about 81% and 64% while such increase is 134% in plain concrete. Because crack-parallel stresses are ubiquitous in practice, the implications for design are significant. **DOI: 10.1061/JENMDT.EMENG-7531.** © *2024 American Society of Civil Engineers.*

Author keywords: Fracture testing; Fiber-reinforced materials; Fracture mechanics; Ductility; Concrete; Crack-parallel stress; Gap test; Fracture process zone (FPZ); Structural failure; Load capacity.

Introduction

The recently developed gap test (Nguyen et al. 2020a) demonstrated that the fracture energy of quasibrittle materials depends strongly on the crack parallel stress, σ_{xx}. In all the classical fracture test specimens such stresses are negligible, and so the σ_{xx} effect is from these specimens undetectable. But in most practical applications such stresses are significant. The gap test implies that the fracture front width is finite and that a triaxial tensorial damage constitutive model must be used to describe quasibrittle fracture (Zhang and Bažant 2023). This indicates that the classical fracture mechanics of line cracks, including the Griffith's type linear elastic fracture mechanics (LEFM) and the cohesive crack model (Griffith 1921; Barenblatt 1962), are merely approcimate reference fracture models underpinning the general fracture model with triaxial damage within a finite crack front width.

Concrete is known to become more brittle as its strength increases (Mansur et al. 1999). To counter it, fiber-reinforced concrete (FRC) has been used to introduce some degree of ductility into the post-peak softening deformation (Mansur et al. 1999; Biolzi et al. 2000; Bencardino et al. 2010). One popular type of concrete fiber suppressing brittleness is the polypropylene (PP) fiber, which is cost-effective, stable in the concrete environment, and has satisfactory mechanical properties (Shafei et al. 2021). Hsie et al. (2008) investigated the mechanical properties of PP hybrid FRC using two types of PP fibers—coarse monofilament and staple fibers. They found that, with the addition of 9 kg/m^3 of the former and 0.6 kg/m^3 of the latter, the splitting tensile strength increased by 13.35%, and the modulus of rupture by 24.60%. Other fibers, such as polyethylene (PE) fiber, steel fiber, and carbon fiber have also been used widely in industry.

Fracture properties of concrete improved by fibers have been analyzed by means of Bažant's size effect law (SEL) (Bažant and Pfeiffer 1987; Bažant et al. 2022a), which describes how the nominal strength of geometrically scaled structures decreases with an increasing structure size (Bažant et al. 2022b; Bažant and Kazemi 1990). The preferred configuration for measuring the initial fracture energy (G_f) and the total fracture energy (G_F) of concrete is a three-point-bend notched beam. Measuring the peak loads obtained for different structure sizes, initial fracture energy (G_f) and the effective size of the FPZ (c_f) can be obtained by Bažant's size effect method (Bažant and Kazemi 1990), which represents the RILEM international standard recommendation TC89-FMT (Bažant 1990b) and was generalized for dissimilar specimens in Bažant and Kazemi (1990). Nguyen et al. (2013) showed that as the size of the specimen decreased, the flexural strength, normalized deflection, and normalized energy absorption

[1]Assistant Research Professor, Advanced Structures and Composites Center, Univ. of Maine, Orono, ME 04468; Dept. of Civil and Environmental Engineering, Univ. of Maine, Orono, ME 04468.

[2]Ph.D. Candidate, Materials Science and Engineering Program, Univ. of Colorado, Boulder, CO 80309. ORCID: https://orcid.org/0009-0006-4294-6752

[3]Graduate Research Assistant, Dept. of Civil and Environmental Engineering, Northwestern Univ., Evanston, IL 60208.

[4]Postdoctoral Researcher, School of Engineering, Brown Univ., Providence, RI 02912.

[5]Professor, Dept. of Civil and Environmental Engineering, Northwestern Univ., Evanston, IL 60208.

[6]Associate Professor, Dept. of Civil, Environmental, and Architectural Engineering, Univ. of Colorado, Boulder, CO 80309; Materials Science and Engineering Program, Univ. of Colorado, Boulder, CO 80309 (corresponding author). ORCID: https://orcid.org/0000-0003-1933-7132. Email: mija.hubler@colorado.edu

Note. This manuscript was submitted on August 24, 2023; approved on November 28, 2023; published online on February 8, 2024. Discussion period open until July 8, 2024; separate discussions must be submitted for individual papers. This paper is part of the ***Journal of Engineering Mechanics***, © ASCE, ISSN 0733-9399.

capacity of ultra-high-performance hybrid FRC increased significantly, whereas the average crack spacing on the bottom surface of the specimen was noticeably decreased. Bencardino et al. (2010) concluded that, in FRC, the size effect generally appeared to be weaker than in plain concrete.

The stress field of σ_{xx} adjacent to the notch is almost uniform, as shown by Nguyen et al. (2020a, b). Analysis of its interaction with the FPZ yielded a nonmonotonic change of G_f and c_f as σ_{xx} increased. In the gap test, which is a modification of the traditional notched three-point-bend (3PB) test, the key difference is that, instead of placing the beam directly on the rigid end supports, two elastoplastic blocks (or pads), here made of polypropylene, are placed next to the notch at the bottom of the beam, whereas the end supports are installed with proper gaps above them before the loading is applied. Polypropylene is used due to its near-perfect yield plateau, which indicates that during fracture growth the force on the pads is almost constant and thus equivalent to a gravity load. Nguyen et al. (2020a, b) showed that a moderate σ_{xx}, about a half of the uniaxial compression strength f_c, approximately doubled the initial fracture energy G_f of plain concrete. These authors opined that a moderate pressure increased static friction on closed inclined microcracks and thus increased the resistance of FPZ to deformation, leading to an increase of G_f. A higher crack-parallel stress that was close to the compression strength limit f_c of the concrete caused, however, slipping on the inclined microcracks, with a friction drop to its dynamic value, which caused axial splitting and lateral expansion of the FPZ (with c_f increase), eventually reducing G_f to zero as f_c is approached (Nguyen et al. 2020b).

Inspired by the previous experiments on plain concrete and the results predicted for FRC by a crack band model with microplane M7f model for fiber reinforced concrete (Nguyen et al. 2020a, b; Caner et al. 2013), it is expected that the crack-parallel stress would have a similar, though milder, effect on the fracture behavior of FRC undergoing sliding, debonding, and fiber stretching. Therefore, in this study, we performed the gap tests on FRC and used the size effect method to analyze them. The experimental data were then compared with the finite element (FE) predictions and to the gap tests on plain concrete.

Materials and Specimen Preparation

To ensure uniform mixing, commercial concrete from Boulder Ready Mix Concrete Inc. was used to cast specimens with a guaranteed minimum compressive strength of 27.58 MPa at 28 days, and a slump of 10 cm. Three different types of concrete were selected: (1) plain concrete (PC), (2) fiber-reinforced concrete (FRC-I) with polyolefin fiber, and (3) fiber-reinforced concrete II with virgin copolymer/polypropylene fiber (FRC-II). The mix design is provided in Table 1 following the ASTM standards ASTM C150-07 (ASTM 2007), ASTM C618-22 (ASTM 2022), ASTM C94/C94M-23 (ASTM 2023), ASTM C494/C494M-17 (ASTM 2017), ASTM C33/C33M-18 (ASTM 2018), and ASTM C260-10 (ASTM 2010). The polyolefin fiber, commercially available as FiberForce 750, has a diameter range from 0.38–0.89 mm and a standard length of 38 mm. The objective of adding this type of fiber is to control microcracks caused by shrinkage and freeze-thaw cycles, and to a limited extent improve the tensile strength of concrete. The virgin copolymer/polypropylene fiber, commercially named FORTA-FERRO, is made of fibrillated and twisted fiber bundles (Nematzadeh and Hasan-Nattaj 2017). Each individual fiber has a diameter of 0.34 mm and a length of 54 mm. Compared with the FiberForce 750, the FORTA-FERRO is mostly applied to improve the tensile strength of concrete and to bridge the macrocracks.

Table 1. Mix design of commercial concrete

Material specification	kg/m^3
Water-to-cement ratio	0.12
ASTM C150–cement	163
ASTM C618–Type C fly ash	18.4
ASTM C94–water	19.6
ASTM C494–Type A water reducer	0.33 low-range + 0.37 midrange
ASTM C33 #67–coarse aggregate	456
ASTM C33 #2–fine aggregate	449
ASTM C260–air entraining agent	0.03
Polyolefin fiber (FRC-I only)	0.59
Virgin copolymer/polypropylene fiber (FRC-II only)	0.59

Three groups of geometrically scaled beam specimens were cast for each type of concrete considering the size guidelines from ASTM E1290-08e1 (ASTM 2008), shown in Fig. 1 and Table 2. The displacement was measured by the machine (MTS 810 hydraulic testing system), which generated the seating effect that appeared at the beginning of the load-displacement curve. To achieve repeatable results, 11 identical beams were prepared for each size and each type of concrete. Six of them were used to conduct the gap test, four were used to conduct the classic notched three-point-bend test, and one was used for a compression test. In addition, three 100×200 mm^2 cylinders and three 100×50 m^2 cylinders were prepared for tensile strength and elastic modulus assessment for each type of concrete mix. The casting was completed within 3 days, with 1-day casting for each type. All the specimens were cured in a moist room at 23°C with a relative humidity of 75% for 56 days until the test. The test for each type of concrete was completed in 2 days.

Polypropylene pads with 25.4 mm thickness were customized to create blocks with different lengths (size 1:60, size 2:30, and size 3:15 mm) and 60 mm width for different beam sizes. A plain weave carbon fiber fabric layer with 2 mm thickness from FIBREGLAST was cut to the sizes of the polypropylene blocks.

Experimental Setup and Procedure

The gap test was developed at Northwestern University by modifying the classic three-point-bend test (Nguyen et al. 2020a). Two polypropylene blocks are placed next to the notch and, symmetrically, two rigid metal blocks of identical cross section are set on the opposite side of the beam, as shown in Fig. 1. To adjust the magnitude of the yield forces of the polypropylene pads, multiple holes of 9.5 mm diameter are drilled through the polypropylene pads. To avoid the risk of stress localization, the distance between holes and edges is larger than the hole diameter. For different sizes of polypropylene pads, about 40% of the total area was drilled. Rigid supports are installed at both ends of the beam with gaps of proper magnitude as calculated.

As the loading process begins, the blocks deform and provide an increasing crack-parallel compressive stress until they reach their yield strength, after which the force applied by the blocks on the specimens becomes constant. The rotation of the fixture that controls the displacement of the pads had to be fixed to avoid uneven deformations of the two blocks. Depending on the gap width, a long stress plateau of yielding may be obtained before the gaps completely close. Before the closing, the middle of the beam is under transverse pure compression until the rigid supports begin to engage, causing the system to switch to a configuration that is again statically determinate because the constant forces from the pads

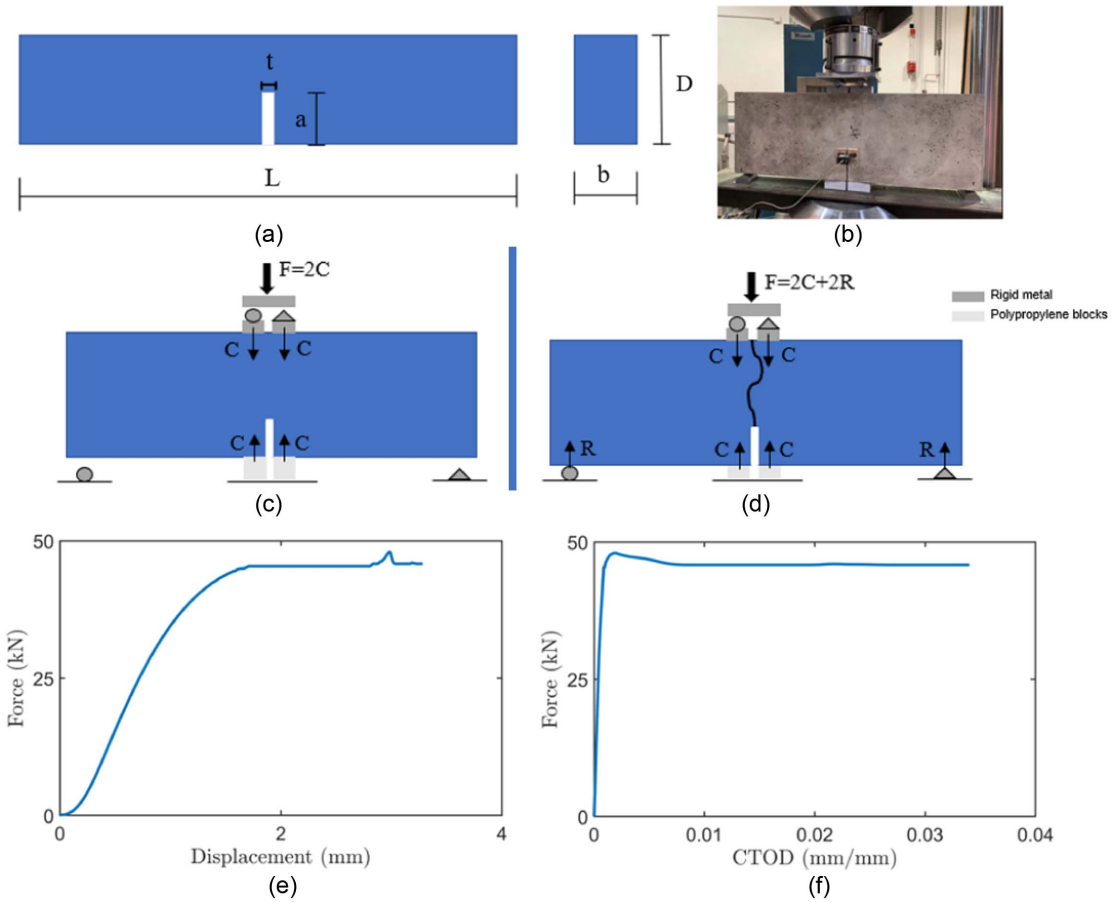

Fig. 1. Schematic of the gap test: (a) beam dimension; (b and c) initial stage of the experiment setup; (d) final stage of the experiment setup: pads yield, the gap between beam and supports is closed, and cracks are generated; (e) force versus displacement: the peak on the plateau is from the gap closing; and (f) force versus crack-tip-opening displacement (CTOD).

Table 2. Dimensions of beam specimens

Size	D (mm)	L (mm)	a (mm)	b (mm)	t (mm)
Small	60	170	20	60	3
Mid	120	340	40	60	3
Large	240	680	80	60	3

Note: D = depth of beam; L = length of beam; a = notch depth; b = width of beam; and t = notch width.

are equivalent to dead loads. The bending introduced by the end support opens the crack (Nguyen et al. 2020b), and the applied load increases again until failure, which occurs of the beam immediately after reaching the maximum load. The experimental configuration is easy to install in beams of different sizes. After repeating the gap test for several sizes, the size effect method is used to evaluate the fracture energy, G_f, and the characteristic FPZ size, c_f, of the material (Nguyen et al. 2020b).

During the test, the loading process was recorded as plotted in Fig. 1. To prevent shear failure of the concrete under the polypropylene pads, the plain weave carbon fiber fabric layer was glued to the bottom surface of the beam. The contribution of the fabric layer to the stress intensity factor and, in general, the mechanical response of the beam is negligible (Nguyen et al. 2020b). The displacement-controlled loading rate was selected so that the maximum loads of the beam with different sizes was reached at approximately the same time. Large-, mid-, and small-size specimens were loaded at load-point displacement rates of 1, 0.5, and 0.25 mm/min, respectively. The crack-tip-opening displacement (CTOD) of each beam was recorded using the clip-on gage. To confirm the effect of crack-parallel stress on fracture energy and fracture process zone size of FRC, the classic three-point-bend test was also performed for comparison.

To fully characterize the mechanical properties of the tested materials and to evaluate the level of crack-parallel stress with respect to their compressive strength, such a property, along with the elastic modulus and tensile strength for each concrete mix, are measured. The compressive strength and elastic modulus were obtained from compression tests [ASTM C39/C39M-14 (ASTM 2014)] and the tensile strength was measured by the Brazilian splitting test, ASTM C496/C496M, (Li et al. 2020). The compression tests were done in two different ways: by using the classic cylinder test following ASTM standard C39 [ASTM C39/C39M-14 (ASTM 2014)] and by placing the beam specimens from the gap test in compression, shown in Fig. 1. The polypropylene blocks from the gap test were replaced with metal blocks for the compression test. Conducting the compression test on the beam specimens provides compressive strengths which include the effects of geometry and confinement of the specimens. The loading rate for the compression test of each specimen size was selected according to the loading rate of the gap test. The cylindrical specimens prepared for the Brazilian split-cylinder test had a diameter of 100 mm and a thickness of 50 mm. The loading rate was fixed at 5 mm/min.

A stress reduction ratio, $r_c = \sigma_{xx}/\sigma_{\text{pad}} \approx 0.96$, was previously observed at the crack front of plain concrete specimens subjected to

crack-parallel stress (Nguyen et al. 2020a, b) (σ_{pad} is the compressive stress under the polypropylene blocks, and σ_{xx} is the real crack-parallel stress measured at the crack front, which is slightly lower). Compared with other fundamental fracture experiments, the gap test had a relatively low success rate (approximately 60%–70%). The cause was primarily the inconsistency of yielding stress level and the appearance of undesired cracks away from the notch.

Size Effect Law (SEL) for Fracture Analysis

Since the dawn of mechanics of materials, the strength criterion was used to assess failure. Griffith (1921) introduced the criterion of linear elastic fracture mechanics (LEFM). In the case of structures made of quasibrittle materials in which the inhomogeneity is not negligible, as in FRC. Neither criterion can adequately describe their fracture behavior. Therefore, the size effect law (SEL) was developed to describe the transition between the two aforementioned asymptotes, which stretches across more than three orders of magnitude. This theory was originally proposed by Bažant and Pfeiffer in 1987 (Bažant and Pfeiffer 1987) and extended to FPZ size estimation by Bažant and Kazemi in 1990 (Bažant and Kazemi 1990). Since then, it has been shown to apply to many other materials (Bažant and Gettu 1992; Bažant and Jirásek 1993; Bažant et al. 1991, 1993; Bažant and Planas 1998). The SEL is here once more used to analyze the fracture properties of both PC and FRC, both with and without crack-parallel stress. The SEL reads

$$\sigma_N = \frac{Bf_t'}{\sqrt{1 + D/D_0}} \tag{1}$$

where σ_N = nominal bending stress for each size of beam; f_t' = tensile strength of the beam; D = depth of the beam; and B and D_0 = two unknown constants by fitting test results for geometrically similar specimens of various sizes

$$\sigma_N = \frac{P_u}{bD} \tag{2}$$

where P_u = ultimate load that the beam can sustain; and b and D = width and depth of the beam. Eq. (1) can be rearranged as a linear relation plot between $1/\sigma_N^2$ versus D (del Viso et al. 2008):

$$\frac{1}{\sigma_N^2} = \frac{1}{B^2 f_t^2} + \frac{D}{B^2 f_t^2 D_0} = > Y = C + AX \tag{3}$$

where $Y =, (1/\sigma_N^2)X = D$. Then

$$G_f = \frac{B^2 f_t^2 D_0 k^2(\alpha)}{E} \tag{4}$$

$$c_f = \frac{D_0 k(\alpha)}{2k'(\alpha)} \tag{5}$$

where G_f = fracture energy; $k(\alpha)$ = shape factor representing the nondimensionalized stress intensity factor; $\alpha = a/D$, = relative crack length; E = elastic modulus of the material; and c_f = size of the fracture process zone (FPZ)

$$k(\alpha) = \frac{1.1682(2l - s)\sqrt{\pi\alpha}}{8\beta^{\frac{3}{2}}}\left(5 - \frac{10\alpha}{3} + \alpha^2 + 40\alpha^2\beta^6 + 3e^{-\frac{6.134\alpha}{\beta}}\right) \tag{6}$$

$$k'(\alpha) = \frac{dk(\alpha)}{d\alpha} \tag{7}$$

where $l = L/2D$ = relative span between the supports; $s = S/D$, = relative distance between the two center-span loads; and $\beta = 1 - \alpha$ (del Viso et al. 2008). Here, c_f characterizes the effective length of the FPZ, but according to the thermodynamics of configurational forces (Bažant 1990a) it also characterizes the width of the FPZ.

Experimental Results

The compressive strengths and the elastic moduli for three different types of commercial concrete are shown in Fig. 2. The compressive strengths recorded from the beam specimens are higher than those obtained from cylindrical specimens. This is because the confinement provided by the sides of the beam elevates the compressive strength. The FRC-II specimens showed the greatest difference between the strengths of beam and of cylindrical specimens. This is due to a significant lateral confinement provided by this type of fiber. The compression tests exhibited the observed size effect. In addition to the confinement, the incorporation of fibers caused some decrease in compressive strength. As more and larger fibers were added, the compressive strength of concrete was observed to decrease, in agreement with (Mansur et al. 1999; Biolzi et al. 2000). FRC-II delivered the lowest compressive strength with the virgin copolymer/polypropylene fibers, which have the largest fiber dimensions. For cylinder samples, there is a 15% compressive strength decrease from PC to FRC-I and a 25% compressive strength decrease from PC to FRC-II. Additionally, with an increase in the size of the beam, the compressive strength of identical material decreased. This size effect has been found and well-established in the past. Considering the confining pressure provided from the side of the beam, the drop of the compressive strength caused by fiber addition amounted to only 4% in comparing PC with FRC-I and 7% in comparing compressive PC with FRC-II. The elastic modulus was calculated from the slope of the initial linear portion of the stress-strain curve.

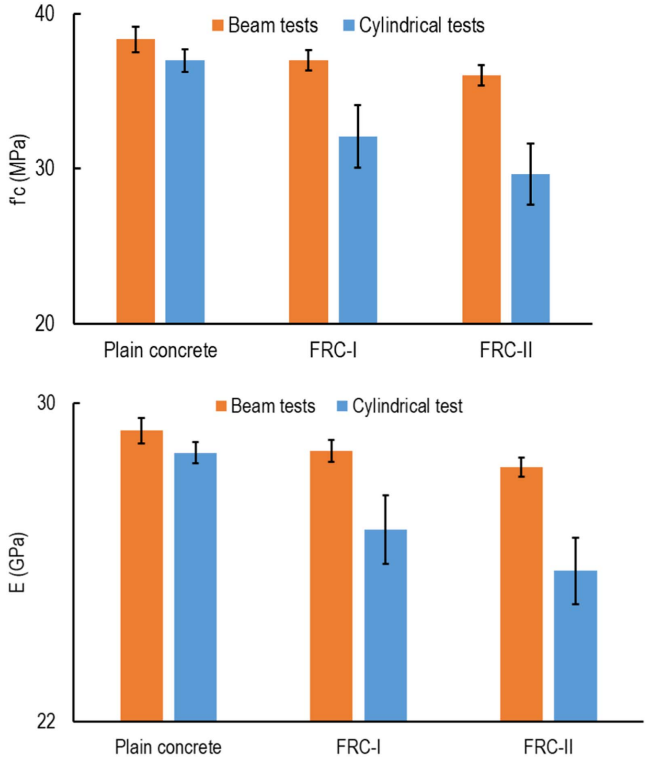

Fig. 2. Compressive strengths and elastic moduli of commercial PC, FRC-I, and FRC-II.

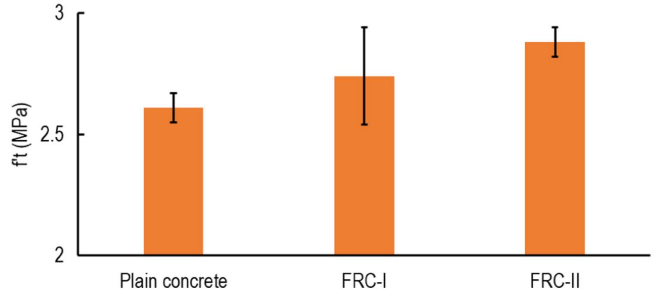

Fig. 3. Tensile strengths of different types of commercial concrete.

The tensile strengths obtained from the Brazilian splitting tests are shown in Fig. 3. As seen, the addition of fiber improves the tensile strength of concrete. A 5% tensile strength increase is achieved from FRC-I samples, and a 10% improvement in tensile strength is found from FRC-II samples.

The key difference between the three-point bending test and the gap test stems from the precompression on the polypropylene pads. These pads represent elastoplastic supports, which introduce the crack-parallel stress σ_{xx} before and during application of the bending moment. To quantify the value of σ_{xx}, FE analysis was conducted by Nguyen et al. (2020a, b). The simulation results showed that an approximate relationship between the σ_{xx}, and the yielding stress of polypropylene pads, σ_{pad}, can be developed, as shown in Eq. (8). From the measured value of, σ_{pad}, one calculates σ_{xx} by using the reduction ratio. The FE elastic analysis provided $r_c = 0.962$, and the crack band FE simulation with microplane models M7 and M7f (Caner et al. 2013; Caner and Bažant 2013) gave 0.942 for the medium size FRC specimens (M7f is an option within the M7 program freely downloadable from the website at Northwestern University), where

$$r_c = \sigma_{xx}/\sigma_{\text{pad}} \tag{8}$$

To avoid the high yield strength of plastic pads, which might be even higher than the compressive strength of concrete, lower yield strengths were obtained by drilling a set of holes in the pads. The stress-strain curve of the pad with holes is provided in Fig. 4. The crack-parallel stress can then be calculated based on the yield strength of plastic pads with a reduction ratio obtained from crack band FE analysis (Nguyen et al. 2020a). It needs to be clarified that the displacement was measured by the testing machine, which caused the seating effect that appeared at the early stage of the nominal strain measurement. The converted crack parallel stress from the yield strength of the plastic pads is listed in Table 3. Besides, to make a direct and clear comparison between the three-point-bend and gap tests, the offsetting process was applied

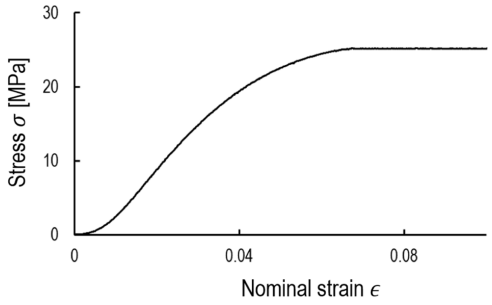

Fig. 4. Stress versus nominal strain curve of plastic pads.

Table 3. Yield strength of polypropylene blocks and crack-parallel stress

Size	σ_{pad} (MPa)	σ_{xx} (MPa)
60×60 mm^2	24.77	23.53
30×60 mm^2	26.12	24.81
15×60 mm^2	27.35	25.98

Table 4. Nominal bending stress (σ_N in MPa) of different types of commercial concrete under different testing methods

Test method	Concrete type	Small beam	Mid beam	Large beam
Three-point test	PC	0.54 ± 0.01	0.45 ± 0.02	0.36 ± 0.01
	FRC-I	0.68 ± 0.05	0.54 ± 0.01	0.45 ± 0.02
	FRC-II	0.70 ± 0.03	0.60 ± 0.03	0.46 ± 0.01
Gap test	PC	0.53 ± 0.07	0.42 ± 0.03	0.29 ± 0.03
	FRC-I	0.61 ± 0.08	0.47 ± 0.05	0.32 ± 0.01
	FRC-II	0.69 ± 0.05	0.50 ± 0.07	0.35 ± 0.03

to the gap test results. The near-horizontal plateau was achieved by compressing the plastic pads. The offsetting point was picked after the beams contacted the rigid support—precisely, with 0.5% of total force increment extracted from the testing data.

Table 4 shows that crack-parallel compression decreases the load capacity of the beams, which is a feature discovered by Nguyen et al. (2020a) while testing the effect on the fracture properties of concrete.

The size effect curves for three-point bend tests of three types of concrete are shown in Figs. 5(a–c), and curves for gap tests are shown in Figs. 6(a–c). To obtain the fracture properties, these data need to be fitted optimally with Eq. (1) using least-square fitting or with Eq. (3) using linear regression [Figs. 5(d) and 6(d)]. An apparent weakening effect due to addition of fibers is found both for the three-point-bend test and from the gap test. Although there are two loading points on the top of the beam, vertically aligned with the pads, they are as close to each other as the pads allow. It would be confusing to speak of four-point bending because in the standard four-point bend test the loads are widely separated, creating a long segment with uniform bending moment and zero shear force.

Analysis and Discussion

The fracture energy and the size of FPZ were calculated from Eqs. (4)–(7). The test results of the effect of crack-parallel stress on the fracture energy are reported in Fig. 7. The fracture energy, G_f, obtained from the gap test on the notched three-point bend beam under moderate compression is larger than that from the standard notched three-point bend beam which has no gaps. The stress ratio (ST) of the crack-parallel stress measured on the polypropylene blocks to the compressive strength of PC ranges from 0.63 to 0.67 depending on the size of the blocks. Fig. 7 illustrates that, with the crack-parallel stress, the fracture energy delivered from the gap test equals about 226% of the fracture energy obtained from the three-point-bend test. For FRC-I and FRC-II, the ST of crack-parallel stress to the compressive strength of FRC ranges from 0.66 to 0.70, and 0.65 to 0.70, respectively. The ST of FRC-I indicates a 64% increment of fracture energy compared with the basic, zero-stress, fracture energy, whereas the ST of FRC-II indicates a 78% increment of the fracture energy compared with the zero-stress fracture energy.

The fibers in the FRC explain the initial weakening of the crack-parallel compression effect on the fracture energy. Specifically, for

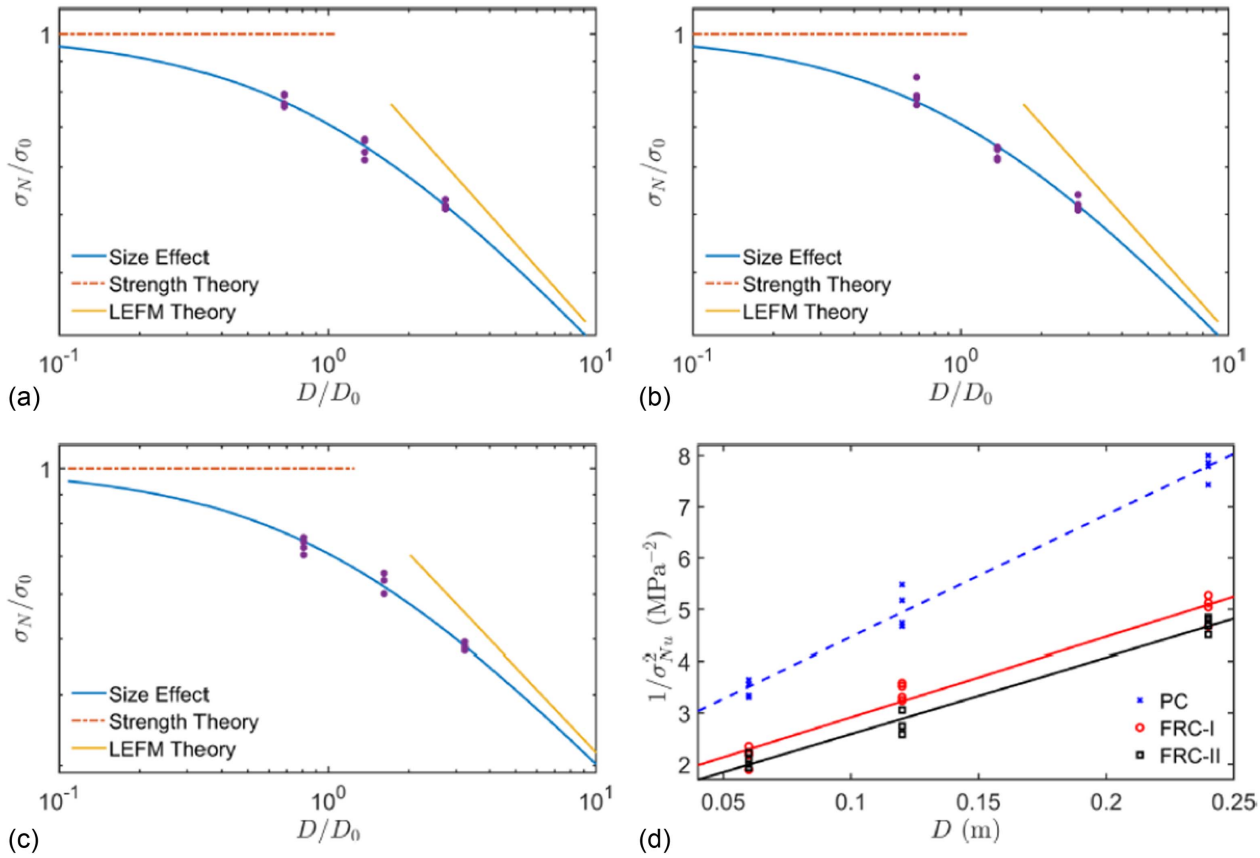

Fig. 5. Size effect curve from three-point bend test: (a) PC; (b) FRC-I; (c) FRC-II; and (d) linear regression curve.

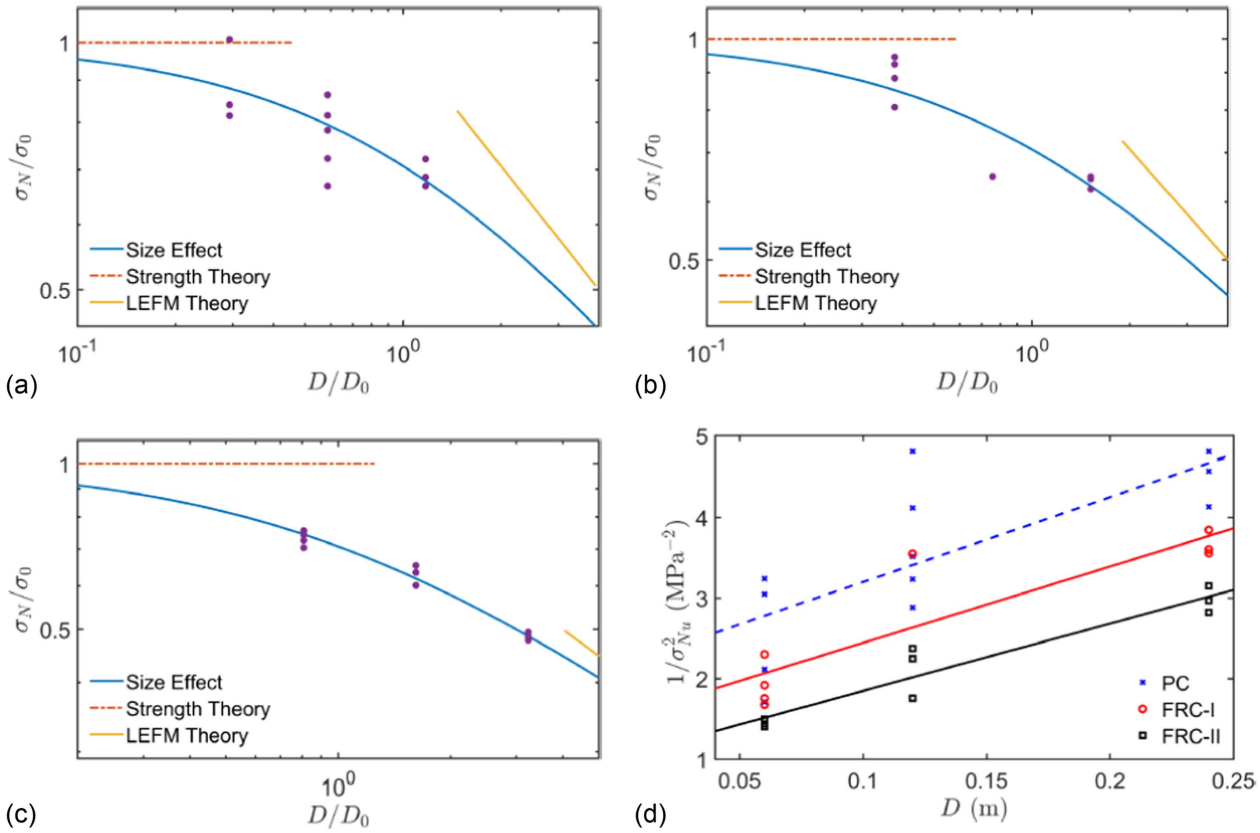

Fig. 6. Size effect curve from gap test: (a) PC; (b) FRC-I; (c) FRC-II; and (d) linear regression curve.

the polyolefin fibers, the increase of fracture energy ratio G_f/G_{f0} was 23% lower than it was for the PC. It appears that adding fiber enhances the cohesive strength and crack bridging effect, which diminishes the fracture energy at low levels of crack-parallel stress. As a result, FRC needs a higher value of crack-parallel compression to attain the same fracture energy increase as the plain concrete.

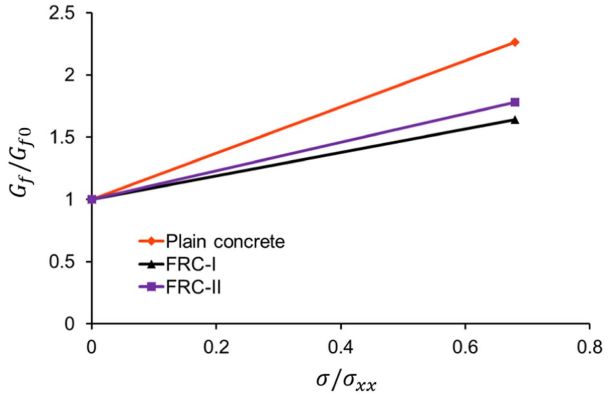

Fig. 7. G_f as a function of crack parallel stress in PC and FRC (normalized by each material's G_{f0} as calculated from standard three-point-bending tests).

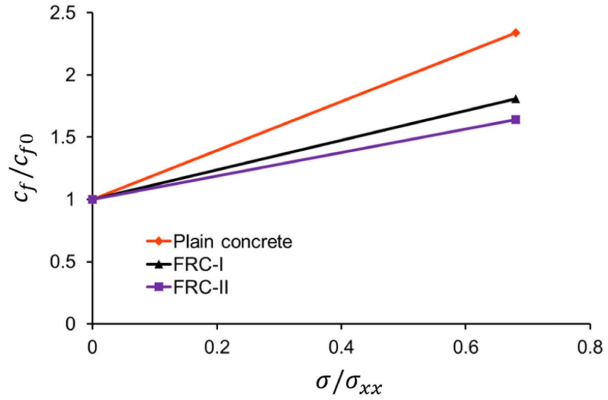

Fig. 8. c_f as a function of crack parallel stress in PC and FRC (normalized by each material's c_{f0}).

The test evaluation by the size effect method (adopted by RILEM in 1990) yields not only the fracture energy G_f but also the effective FPZ size c_f. In the analytical derivation of the size effect method by two-sided asymptotic matching (Bažant and Kazemi 1990; Bažant et al. 2022b), the FPZ was considered as a cohesive zone of finite length but a zero width, as if it were a cohesive line crack. For an FPZ of finite width, the analytical asymptotic-matching derivation would not have been feasible. However, from the thermodynamics of configurational forces (Bažant 1990a; Bažant and Cedolin 1991) it is known that the crack extension has asymptotically the same effect as the crack widening. Therefore, the c_f obtained by the size effect method characterizes both the length and the width of the FPZ, and thus is better called the effective FPZ size.

The effect of crack-parallel stress on the FPZ size is seen in Fig. 8. The ratio of the FPZ size obtained from the gap test to the FPZ size obtained from the standard three-point-bend test is seen on the Y-axis to be significantly larger than 1.0 for all the test data. On the other hand, the addition of fibers to concrete is seen to cause the FPZ size to decrease. Thus, the effects of the crack-parallel stress and of the fibers are competing. Various combinations of these two effects increase or decrease the FPZ size, and the fracture energy value.

Nguyen et al. (2020a, b) conducted a numerical FE investigation on the effect of crack-parallel stress on fracture energy. Different models were applied to simulate the effect on both PC and FRC. The figure verifies that the LEFM (Griffith 1921) and CCM (Barenblatt 1959, 1962) cannot capture the effect of crack-parallel stress and thus are inapplicable except when the crack-parallel stress is zero, which is rare in practice. The discrete crack model similarly cannot capture the triaxial effect on fracture shown here (Etse et al. 2012). On the other hand, the crack band model with the microplane damage constitutive law M7 captures the effect of crack-parallel stress on fracture energy quite well. The solid lines shown in Fig. 8 are the simulation results from the M7 CBM model for PC and FRC (Nguyen et al. 2020a). Fiber-reinforced concrete with 3% Dramix fibers (Nguyen et al. 2020b) was considered in the simulation. The following comparison is made between the test data (dots) and the modeling predictions (lines). These predictions capture the increase of fracture energy ratio (G_f/G_{f0}) with increasing crack-parallel stress obtained from the test data. The small deviations are probably due to the concrete mix design, fiber type, and fiber amount. Values somewhat smaller than experimental ones are seen (on the Y-axis of Fig. 9) are similar to the results from the FE computations with the CBM. Apparently, this is not due to an error of M7. Rather it is due to the widening of the crack band caused by

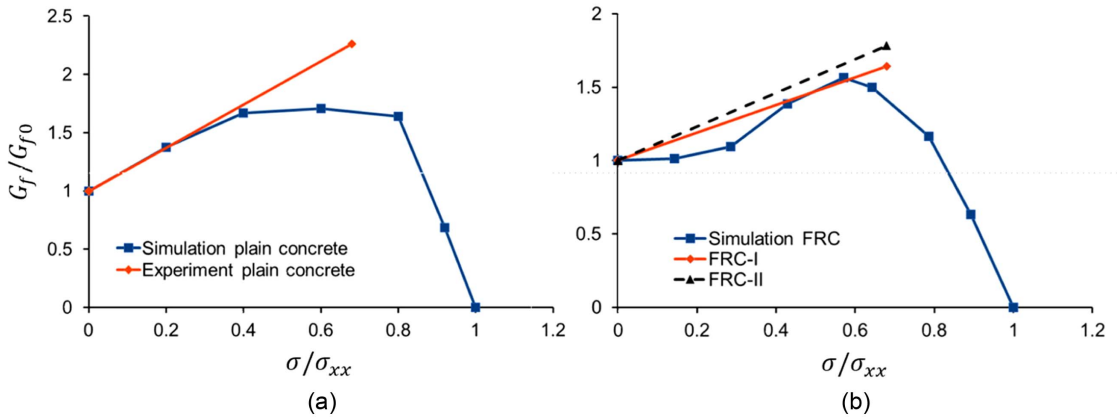

Fig. 9. G_f as a function of crack parallel stress in: (a) PC, normalized by $G_f(\text{plain concrete}) = 26.7$ J/m^2; and (b) FRC, normalized by $G_f(\text{FRC-I}) = 40.9$ J/m^2 and $G_f(\text{FRC-II}) = 42.7$ J/m^2.

crack-parallel compression, as predicted by the theory of smooth crack band model (sCBM) based on the new concept of sprain energy (Zhang and Bažant 2023).

There are various interesting consequences for structural design. For example, in the arguments of supporting the current model code equations for the shear of beams made of plain concrete longitudinally reinforced by steel bars, it was assumed that the load capacity depended on the cohesive stresses along the crack and that, at maximum load, the cohesive stress concentrated into a stress singularity at the tip of that crack. However, at maximum load, the compressive stress in the *compression strut* parallel to the crack reaches the compression strength limit and so, according to Fig. 9, there is, in fact, no stress singularity. Here, one must infer that the same must be true for beams made of FRC reinforced by longitudinal steel bars. Hence, not only for reinforced plain concrete but also for steel reinforced FRC, the beam shear failure is caused by the compression strut, which is what must cause the Type 2 size effect.

Conclusions

1. Two commercial-type fiber-reinforced concretes, labeled as FRC-I and FRC-II, have been studied. The experiments showed that the crack parallel compressive stresses of 0.63 and 0.67 of average standard uniaxial compression strength f_c caused the fracture energy G_f of FRC-I and FRC-II to increase by 64% and 78%, respectively, whereas for plain concrete the increase is 126%.
2. The corresponding crack-parallel stress effect on the effective size of the fracture process zone (FPZ) is increased by 134%, 81%, 64% for PC, FRC-I, and FRC-II, respectively. The small difference between FRC-I and FRC-II is primarily caused by differences in the sizes and tensile performances of the fibers, and in the strength of the bond between fiber and concrete,
3. The fracture energy increase due to crack-parallel compression is for FRC only slightly smaller than it is for plain concrete.
4. Whereas the maximum G_f increase due to crack-parallel compression is large, it is slightly less than the maximum increase of fracture energy for plain concrete of the same type. This shows that the fiber reinforcement mitigates the effect of crack-parallel stress on the fracture energy only slightly, likewise for the effective FPZ size. The ductility of the beam is slightly enhanced by the crack-parallel compression.
5. However, for crack-parallel compression less than about 25% of the compression strength, the effect of fiber reinforcement is insignificant. There is no change in Gf in the case of FRC, whereas for plain concrete the effect is strong.
6. The fiber reinforcement introduces a certain degree of ductility in the load-deflection diagram.
7. Separate FE simulations with the crack band model based on the M7f microplane damage constitutive model for fiber reinforced concrete predicted a qualitatively similar response, but the maximum increase of G_f was underestimated. The reason probably is that the crack front width varies, whereas in the crack band model it is fixed. For plain concrete, the same discrepancy was observed before [this could be remedied by the recently published smooth crack band model (Zhang and Bažant 2023), which yields a variable crack front width].

Data Availability Statement

Experimental data that support the findings of this study are available from the corresponding author upon reasonable request.

Acknowledgments

Support from the University of Colorado Boulder, directed by M. Hubler, is gratefully appreciated. Collaborative work at Northwestern University was supported under US National Science Foundation NSF Division of Civil, Mechanical, and Manufacturing Innovation grant 1439960 to that university. We also thank Mohammed Zainy, M. Scott Cusack, Cory Ihnotic, Katherine O'Dell, Dr. Yao Wang, and Dr. Sannidhya Ghosh from the University of Colorado, Boulder, for assistance with molds designing, specimen casting, and testing setup.

Author contributions: Linfei Li: Investigation, Testing, Writing—original draft, Formal analysis. Boning Wang: Investigation. Houlin Xu: Data curation, Analysis of data. Hoang T. Nguyen: Basic concept —Writing—review and editing, Testing methodology. Zdeněk P. Bažant: Basic concept—Writing—original draft, review and editing, Methodology, Supervision, Funding acquisition. Mija H. Hubler: Basic concept—Writing —review and editing, Methodology, Supervision, Funding acquisition.

References

ASTM. 2007. *Standard specification for portland cement*. ASTM C150-07. West Conshohocken, PA: ASTM.

ASTM. 2008. *Standard test method for crack-tip opening displacement (CTOD) fracture toughness measurement (withdrawn 2013)*. ASTM E1290-08e1. West Conshohocken, PA: ASTM.

ASTM. 2010. *Standard specification for air-entraining admixtures for concrete*. ASTM C260-10. West Conshohocken, PA: ASTM.

ASTM. 2014. *Standard test method for compressive strength of cylindrical concrete specimens*. ASTM C39/C39M-14. West Conshohocken, PA: ASTM.

ASTM. 2017. *Standard specification for chemical admixtures for concrete*. ASTM C494/C494M-17. West Conshohocken, PA: ASTM.

ASTM. 2018. *Standard specification for concrete aggregates*. ASTM C33/C33M-18. West Conshohocken, PA: ASTM.

ASTM. 2022. *Standard specification for coal fly ash and raw or calcined natural pozzolan for use in concrete*. ASTM C618-22. West Conshohocken, PA: ASTM.

ASTM. 2023. *Standard specification for ready-mixed concrete*. ASTM C94/C94M-23. West Conshohocken, PA: ASTM.

Barenblatt, G. I. 1959. "The formation of equilibrium cracks during brittle fracture, general ideas and hypothesis, axially symmetric cracks." [In Russian.] *Prikl. Mekh. Matem.* 23 (3): 434–444. https://doi.org/10.1016/0021-8928(59)90157-1.

Barenblatt, G. I. 1962. "The mathematical theory of equilibrium cracks in brittle fracture." *Adv. Appl. Mech.* 7 (Jan): 55–129. https://doi.org/10.1016/S0065-2156(08)70121-2.

Bažant, Z. P. 1990a. "Justification and improvement of Kienzler and Herrmann's estimate of stress intensity factors of cracked beam." *Eng. Fract. Mech.* 36 (3): 523–525. https://doi.org/10.1016/0013-7944(90)90298-U.

Bažant, Z. P. 1990b. "Size effect method for determining fracture energy and process zone size of concrete (RILEM Recommendation TC89-FMT S.P. Shah, Chair of Committee FMT)." *Mater. Struct.* 23: 461–465. https://doi.org/10.1007/BF02472030.

Bažant, Z. P., and L. Cedolin. 1991. *Stability of structures: Elastic, inelastic, fracture and damage theories*. 1st ed. Oxford, UK: Oxford University Press.

Bažant, Z. P., A. A. Dönmez, and H. T. Nguyen. 2022a. "Précis of gap test results requiring reappraisal of line crack and phase-field models of fracture mechanics." *Eng. Struct.* 250 (Jan): 113285. https://doi.org/10.1016/j.engstruct.2021.113285.

Bažant, Z. P., and R. Gettu. 1992. "Rate effects and load relaxation in static fracture of concrete." *ACI Mater. J.* 89 (5): 456–468. https://doi.org/10.14359/2400.

Bažant, Z. P., R. Gettu, and M. T. Kazemi. 1991. "Identification of nonlinear fracture properties from size effect tests and structural analysis

based on geometry-dependent *R*-curves." *Int. J. Rock Mech. Min. Sci. Geomech. Abstr.* 28 (1): 43–51. https://doi.org/10.1016/0148-9062(91)93232-U.

Bažant, Z. P., and M. Jirásek. 1993. "*R*-curve modeling of rate and size effects in quasibrittle fracture." *Int. J. Fract.* 62 (Aug): 355–373. https://doi.org/10.1007/BF00017241.

Bažant, Z. P., and M. T. Kazemi. 1990. "Determination of fracture energy, process zone length and brittleness number from size effect, with application to rock and concrete." *Int. J. Fract.* 44 (Jul): 111–131. https://doi.org/10.1007/BF00047063.

Bažant, Z. P., J. L. Le, and M. Salviato. 2022b. *Quasibrittle fracture mechanics and size effect: A first course*. Oxford, UK: Oxford University Press.

Bažant, Z. P., and P. A. Pfeiffer. 1987. "Determination of fracture energy from size effect and brittleness number." *ACI Mater. J.* 84 (6): 463–480. https://doi.org/10.14359/2526.

Bažant, Z. P., and J. Planas. 1998. *Fracture and size effect in concrete and other quaibrittle materials*. 1st ed. Boca Raton, FL: CRC Press.

Bažant, Z. P., B. Shang-Ping, and G. Ravindra. 1993. "Fracture of rock: Effect of loading rate." *Eng. Fract. Mech.* 45 (3): 393–398. https://doi.org/10.1016/0013-7944(93)90024-M.

Bencardino, F., L. Rizzuti, G. Spadea, and R. N. Swamy. 2010. "Experimental evaluation of fiber reinforced concrete fracture properties." *Composites, Part B* 41 (1): 17–24. https://doi.org/10.1016/j.compositesb.2009.09.002.

Biolzi, L., S. Cattaneo, and G. L. Guerrini. 2000. "Fracture of plain and fiber-reinforced high strength mortar slabs with EA and ESPI monitoring." *Appl. Compos. Mater.* 7 (Jan): 1–12. https://doi.org/10.1023/A:1008948125654.

Caner, F. C., and Z. P. Bažant. 2013. "Microplane model M7 for plain concrete. I: Formulation." *J. Eng. Mech.* 139 (12): 1714–1723. https://doi.org/10.1061/(ASCE)EM.1943-7889.0000570.

Caner, F. C., Z. P. Bažant, and R. Wendner. 2013. "Microplane model M7f for fiber reinforced concrete." *Eng. Fract. Mech.* 105 (Jun): 41–57. https://doi.org/10.1016/j.engfracmech.2013.03.029.

del Viso, J. R., J. R. Carmona, and G. Ruiz. 2008. "Shape and size effects on the compressive strength of high-strength concrete." *Cem. Concr. Res.* 38 (3): 386–395. https://doi.org/10.1016/j.cemconres.2007.09.020.

Etse, G., A. Caggiano, and S. Vrech. 2012. "Multiscale failure analysis of fiber reinforced concrete based on a discrete crack model." *Int. J. Fract.* 178 (Jun): 131–146. https://doi.org/10.1007/s10704-012-9733-z.

Griffith, A. 1921. "The phenomena of rupture and flow in solid." *Philos. Trans. R. Soc. London, Ser. A* 221 (Jan): 582–593. https://doi.org/10.1098/rsta.1921.0006.

Hsie, M., C. Tu, and P. S. Song. 2008. "Mechanical properties of polypropylene hybrid fiber-reinforced concrete." *Mater. Sci. Eng., A* 494 (1–2): 153–157. https://doi.org/10.1016/j.msea.2008.05.037.

Li, L., M. H. Hubler, and Y. Xi. 2020. "Modeling the corrosion of steel casing and the damage of well cement in a borehole system." *Constr. Build. Mater.* 259 (Oct): 119701. https://doi.org/10.1016/j.conbuildmat.2020.119701.

Mansur, M. A., M. S. Chin, and T. H. Wee. 1999. "Stress-strain relationship of high-strength fiber concrete in compression." *J. Mater. Civ. Eng.* 11 (1): 21–29. https://doi.org/10.1061/(ASCE)0899-1561(1999)11:1(21).

Nematzadeh, M., and F. Hasan-Nattaj. 2017. "Compressive stress-strain model for high-strength concrete reinforced with forta-ferro and steel fibers." *J. Mater. Civ. Eng.* 29 (10): 04017152. https://doi.org/10.1061/(ASCE)MT.1943-5533.0001990.

Nguyen, D. L., D. J. Kim, G. S. Ryu, and K. T. Koh. 2013. "Size effect on flexural behavior of ultra-high-performance hybrid fiber-reinforced concrete." *Composites, Part B* 45 (1): 1104–1116. https://doi.org/10.1016/j.compositesb.2012.07.012.

Nguyen, H. T., M. Pathirage, G. Cusatis, and Z. P. Bažant. 2020a. "Gap test of crack-parallel stress effect on quasibrittle fracture and its consequences." *J. Appl. Mech.* 87 (7): 071012. https://doi.org/10.1115/1.4047215.

Nguyen, H. T., M. Pathirage, M. Rezaei, M. Issa, G. Cusatis, and Z. P. Bažant. 2020b. "New perspective of fracture mechanics inspired by gap test with crack-parallel compression." *Proc. Natl. Acad. Sci.* 117 (25): 14015–14020. https://doi.org/10.1073/pnas.2005646117.

Shafei, B., M. Kazemian, M. Dopko, and M. Najimi. 2021. "State-of-the-art review of capabilities and limitations of polymer and glass fibers used for fiber-reinforced concrete." *Materials* 14 (2): 409. https://doi.org/10.3390/ma14020409.

Zhang, Y., and Z. P. Bažant. 2023. "Smooth crack band model—A computational paragon based on unorthodox continuum homogenization." *J. Appl. Mech.* 90 (4): 041007. https://doi.org/10.1115/1.4056324.